A Powerful Three-dimensional C-F-Bi Cathode for Zn-CO_2 Battery

Shipeng Zhang[a], Xiang Fei[b], Dewen Song[a], Peijin Bai[a], He Kang[c], Wenting Wu[a], Qingshan Zhao[a], Fuwei Xian[d], Hui Ning[a]& Mingbo Wu[ae]*

a State Key Laboratory of Heavy Oil Processing, Shandong Key Laboratory of Advanced Electrochemical Energy Storage Technologies, College of Chemistry and Chemical Engineering, China University of Petroleum, Qingdao, Shandong, 266580

b Yantai Port Pipeline Transportation Co., LTD, Yantai, China, 264001

c College of Chemical and Biological Engineering, Shandong University of Science and Technology, Qingdao, 266590, China

d Qingdao Haier Refrigerator Co., LTD, Qingdao, China, 266100

e State Key Laboratory of Advanced Optical Polymer and Manufacturing, College of Chemical Engineering, Technology Qingdao University of Science & Technology, Qingdao, China, 266061

*Corresponding author. E-mail: ninghui@upc.edu.cn (H. Ning)

1 Experiment

1.1 Materials

All chemicals and reagents were purchased from Sinopharm Holdings Chemical Reagents except otherwise stated. Zinc(II) acetate dihydrate ($Zn(Ac)_2 \cdot 2H_2O$, CAS No: 5970-45-6, ≥98.0%purity) was obtained from Ward's Science. Nafion N117 membrane (0.180 mm thick, exchange capacity 0.90 meq/g) was provided by Alfa Aesar China Co. Ltd. The water in all experiments was purified with the Millipore system. The gases used are all high-purity gases, such as high-purity Ar (99.999%), high-purity N_2 (99.999%), and high-purity CO_2 (99.999%).

1.2 Characterization

The crystal property and phase composition of all the materials as prepared were investigated by X-ray diffraction (X'Pert PRO MPD, Holland) with Cu Ka radiation (λ = 0.15406 nm). The morphology of catalysis was investigated by field emission scanning electron microscopy (FE-SEM, Hitachi S-4800, Japan). Transmission electron microscopy (TEM, JEM2100UHR, Japan) and the high-resolution transmission electron microscope (HRTEM) combined with an energy

dispersive spectrometer (EDS) were used to identify the crystal lattices and elements distribution of the samples. The elemental composition and valence in the materials as-made are analyzed by X-ray photoelectron spectroscopy (XPS, Escalab 250Xi, UK) with an Al Ka X-ray source gun. The static water contact angle was measured by Drop Shape Analyzer (KRüSS DSA25E, Germany). All spectra were collected in ambient conditions.

1.3 Electrochemical measurements

The electrochemical reduction of CO_2 reactions was carried out in an H-type electrolytic cell connected with an electrochemical workstation (CS3004，CORRTEST, China) at room temperature and atmospheric pressure. The two chambers of the cell were separated by a cation exchange membrane (Nafion® N117, DuPont) and filled with 30 mL of 0.1 M $KHCO_3$ as electrolyte. A piece of platinum sheet (1×1 cm^2) was used as the counter electrode and a KCl-saturated Ag/AgCl electrode was used as the reference electrode. For each CO_2 reduction experiment, the 0.1 M $KHCO_3$ solution was saturated with high-purity CO_2 (≥ 99.999%) for 30 minutes until saturated (pH = 6.8). A mass flowmeter was fixed before the cathodic compartment to control CO_2 gas flow at 20 mL min^{-1} and the solution was stirred at 500 rpm.

All the CO_2 reduction experiments were performed under galvanostatic mode and the operating potentials were calibrated to the reversible hydrogen electrode (RHE) using the formula：

E (versus RHE) = E (versus Ag/AgCl) + 0.197V + 0.0591 × pH[1].

The Faraday efficiencies of all products were calculated according to the following equation[2].

$FE = \alpha \times n \times F/Q$

(α: moles of the product; n: transferred electron number; F: Avogadro constant; Q: electric quantity.)

The electrochemical reduction of CO_2 reactions in a flow cell used the same electrochemical workstation, anode, and reference electrode. The cathode was sandwiched between a gas phase plate and a liquid phase plate to form a cathode chamber. Similarly, a platinum sheet (2× 2.5 cm) was sandwiched between a liquid phase plate and a solid plate from anode chamber. The cathode and anode chamber were divided by a bipolar membrane (BPM, 2× 2 cm). The CO_2 gas flow rate was fixed at 50 sccm. The catholyte and anolyte were both 1 M KOH with a flow rate of 10 sccm. The CO_2 gas flows from top to bottom, while the liquid phase KOH does the opposite. Polarization curves were collected at a scan rate of 10 mV $\cdot s^{-1}$. All potential readings were measured against

Ag/AgCl and converted to RHE.

The laser system employs a carbon dioxide laser with a wavelength of 10.6 micrometers. The etching process is conducted in an air environment, operating point-by-point at a speed of 1 centimeter per second over a 5×5 square centimeter area for a duration of 20 minutes.

1.4 Analysis of products

The liquid products were measured using the high-performance liquid chromatograph (LC-2030 Plus, Shimadzu, Japan), configured with a single chromatographic column (SH1011, Shodex, Japan) and a refractive index detector (RID-20A). The operating temperature of the ion exclusion column was 45 ℃ and the mobile phase was 5 mM H_2S_2 solution at a flow rate of 0.5 mL $\cdot min^{-1}$.

The gas-phase products were detected by gas chromatograph (BFRL-3420A, China), using high purity Ar (≥99.999%) as carrier gas. The GC system was online and connected with the headspace of the cathodic compartment. The thermal conductivity detector (TCD) and the flame ionization detector (FID) were installed to quantify hydrogen and carbon-containing products, respectively. The Faradaic efficiencies of all the products were calculated as reported[3].

1.5 BET measurements

Surface areas and pore size distributions were measured by nitrogen adsorption and desorption at 77.3 K using a Micromeritics ASAP 2020 volumetric adsorption analyzer. Samples were degassed at 110 °C for 15 h under vacuum (10-5 bar) before analysis. To calculate the BET specific surface area, the standard pressure range of 0.05~0.20 was selected to obtain high regression coefficient BET linearization (≥0.999)[4], which was transferred from BET equation:[5]

$$\frac{p/p_0}{n\left(1 - p/p_0\right)} = \frac{1}{n_m C} + \frac{C - 1}{n_m C}\left(p/p_0\right)$$

where n is the specific amount of the adsorbed gas at the relative pressure p/p_0, n_m is the monolayer capacity of the adsorbed gas, p is the pressure, p_0 is the saturation pressure of a substance being adsorbed at the adsorption temperature, and C is the BET constant which is exponentially related to the energy of monolayer adsorption.

The *t*-plot method conducted by the statistical thickness of the adsorption film relative to the adsorption amount, which was used to estimate the volume and surface area of micropores. As the average monolayer thickness of nitrogen is 0.354 nm, the thickness of nitrogen adsorption layer (*t*) could be calculated by Harkins and Jura equation.[6] And date in the p/p_0 range of 0.3~0.6 were

selected to linear fitting. Barrett, Joyner and Halenda (BJH) theory was used to calculate the pore size distribution curves of samples. The equilibrium relationship between adsorption layer thickness and pressure based on Halsey equation with Faas correction.[7] All the linear fitting results were satisfied with high regression coefficient over 0.999.

1.6 ECSA measurements

The electrochemically active surface area (ECSA) of the catalyst was measured by the double-layer capacitance method. The electrochemical capacitance was determined by measuring the non-Faradaic capacitive current associated with the double-layer charging from the scan-rate dependent cyclic voltammograms. The relationship of double-layer charging current jc, the scan rate v, and the electrochemical double-layer capacitance Cdl is given in equation.

$$jc = v \times Cdl \quad (1)$$

From equation (1), Cdl can be obtained by plotting ic as a function of v. Then, the ECSA can be calculated from the double layer capacitance Cdl and the specific capacitance Cs using equation (2).

$$ECSA = Cdl/Cs \quad (2)$$

From equation (2), it can be seen that the ECSA is proportional to the double layer capacitance Cdl.For experiment details, the CV curves was collected from -0.25 to -0.35 V vs. RHE with various scan rates of 20, 40, 60, 80 and 100 mV s^{-1}. The IR compensation operation for was conducted as mentioned above. The Cdl was estimated by plotting the $\triangle(j_a-j_b)/2$ at -0.2 V vs. RHE against the scan rate, in which ja and jb were the anodic and cathodic current density, respectively. The linear slope was equivalent to Cdl and R^2 of fitting lines above 0.999.

2 Theoretical calculations

All the theoretical calculations were performed using Vienna ab initio simulation packages (VASP). The Perdew-Burke-Ernzerhof (PBE) functional was used to describe the exchange-correlation term between electrons based on the generalized gradient approximation (GGA). The plane wave energy cut-off was set to 400 eV. The Brillouin zone was sampled by a 2×2×1 Monkhorst-Pack K-points sampling for structural optimizations. A vacuum of 15 Å in the z direction was employed to avoid interactions between periodic images. The criterion of energy convergence was 1×10^{-5} eV. The calculation of adsorption-free energy was defined as the equation: Eads = E(total) – E(surface) – E(isolated adsorbate).[8] The Gibbs free energy for each reaction pathway in

CRR can be calculated as a flowing equation: $\Delta G = \Delta Eads + \Delta ZPE – T\Delta S$.[9] Where Eads was the electronic adsorption energy in the self-consistent calculation, and ZPE stood for the zero-point energy difference between adsorbed and gaseous species while S was the enthalpy in the process.

3 Supporting Figures and Tables

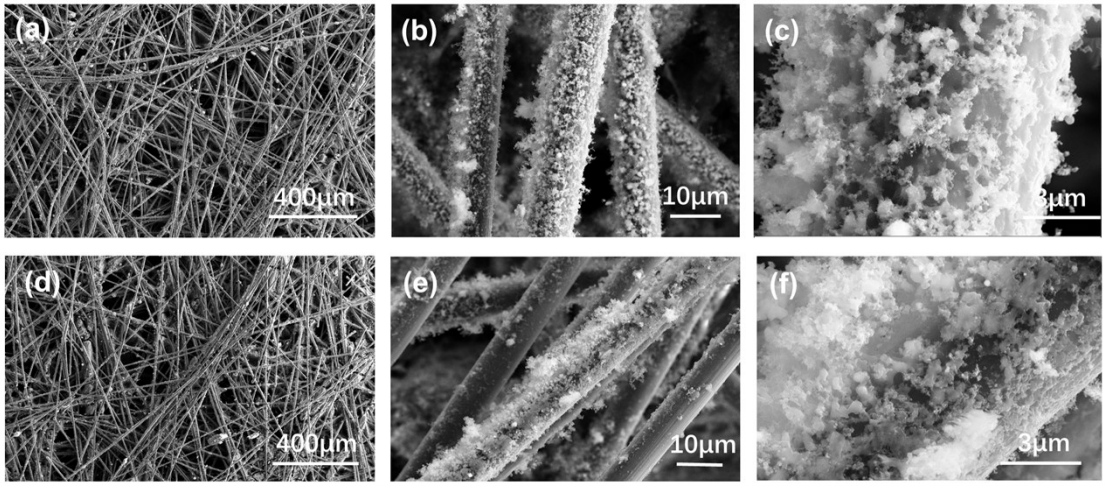

Figure S1. SEM images of (a) (b) (c) Bi-F@C 3DSSE-7W, (d) (e) (f) Bi-F@C 3DSSE-3W.

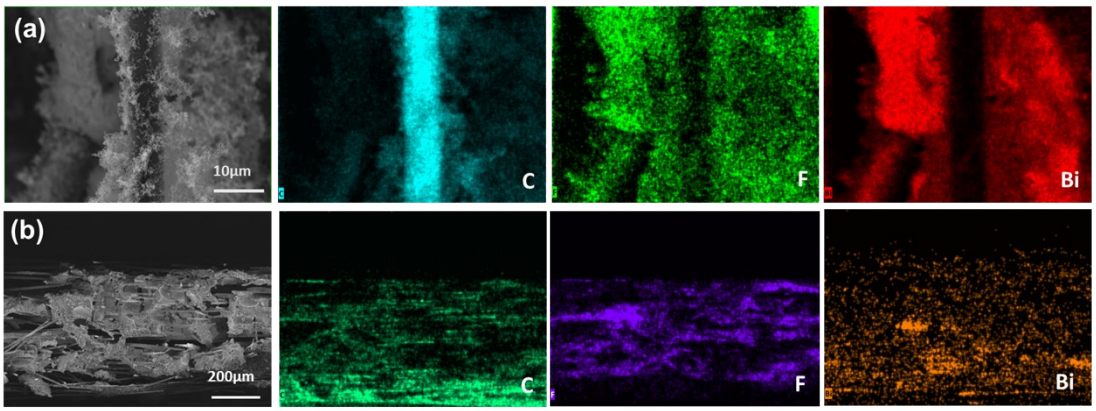

Figure S2. The HAADF-STEM (a) and cross-section HAADF-STEM (b) image of Bi-F@C 3DSSE with corresponding EDS mapping.

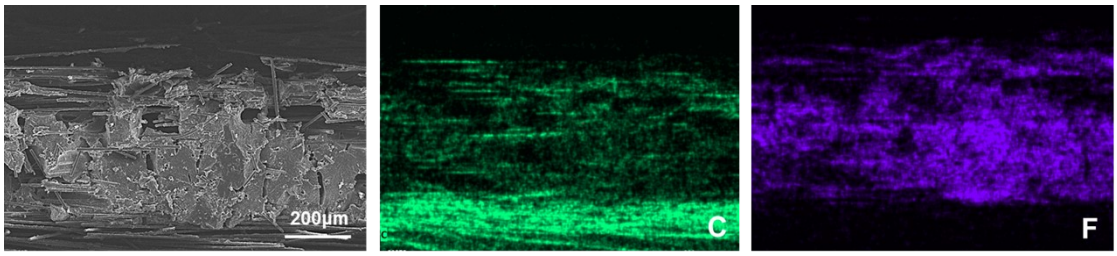

Figure S3. HAADF-STEM image and corresponding EDS mapping of F@C 3DSSE.

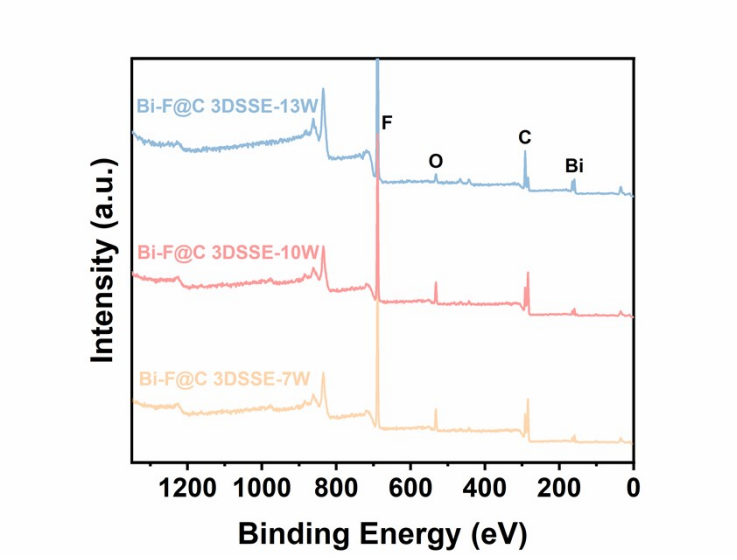

Figure S4. XPS survey spectrum of the Bi-F@C 3DSSE.

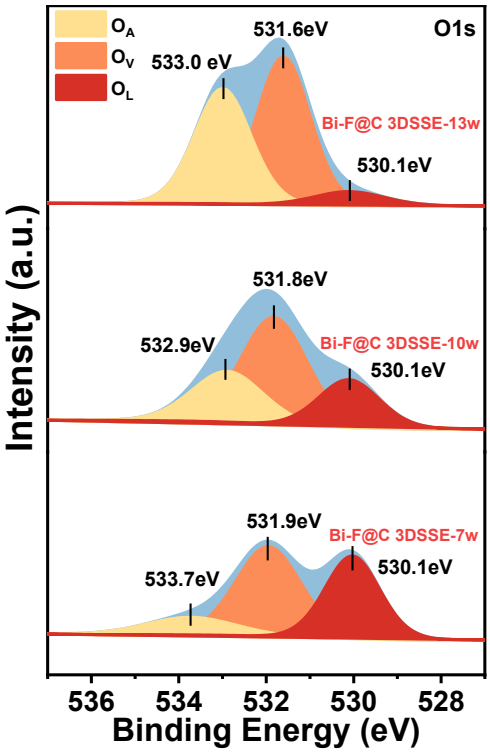

Figure S5. High-resolution O1s spectrum of the Bi-F@C 3DSSE.

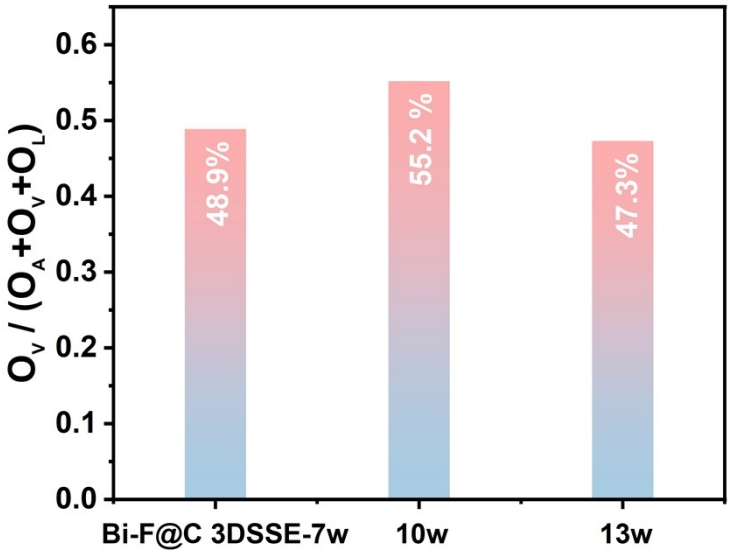

Figure S6. Comparison of the $O_V/(O_A+O_V+O_L)$ ratio among various catalysts.

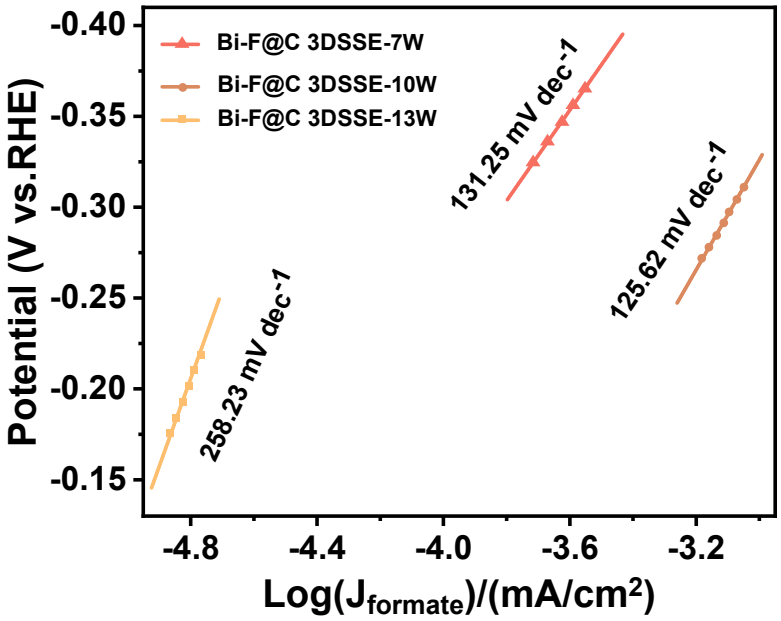

Figure S7. The Tafel plots of different materials.

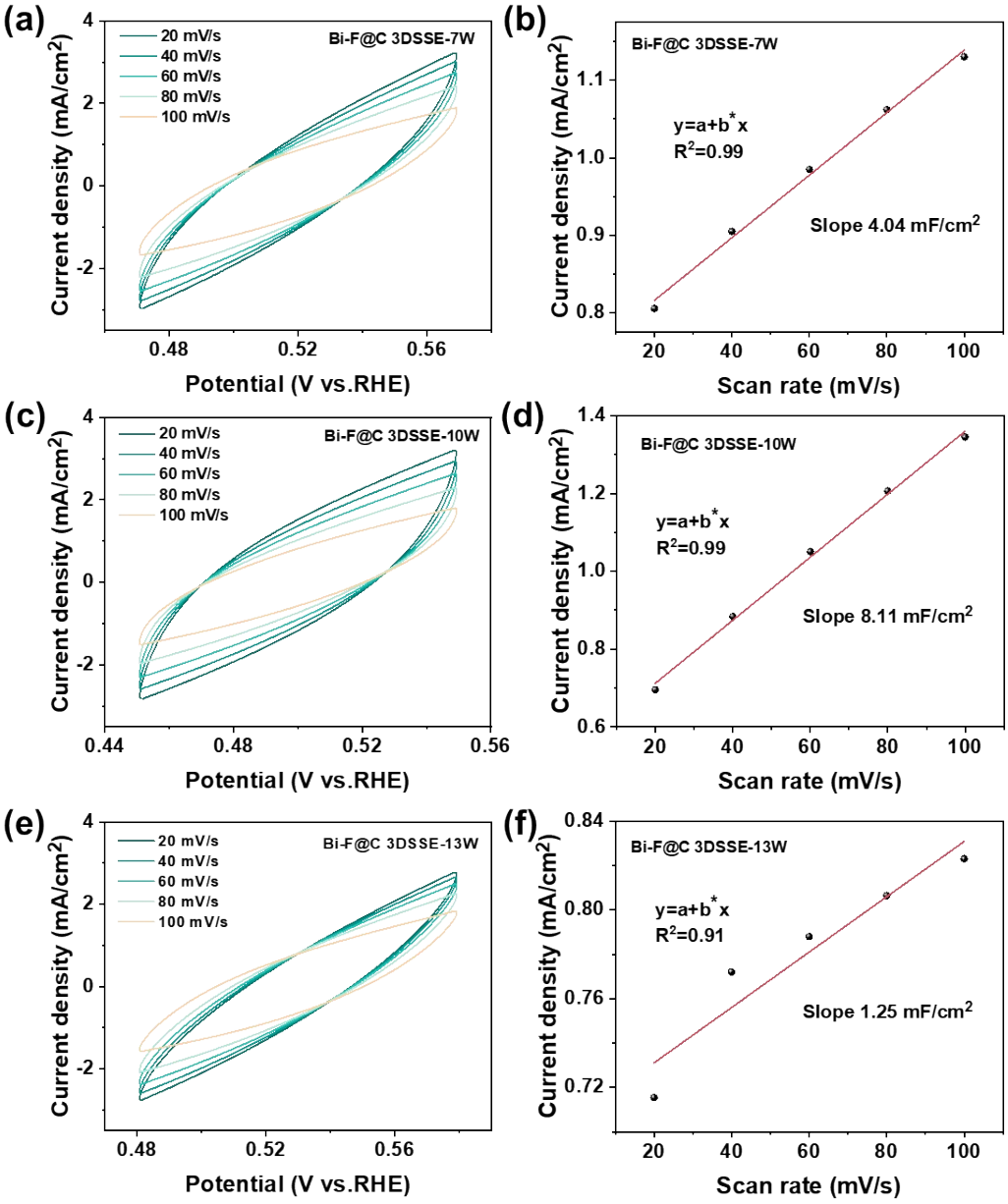

Figure S8. The CV curves of (a) Bi-F@C 3DSSE-7W, (b) Bi-F@C 3DSSE-10W and(c) Bi-F@C 3DSSE-13W. The charging current density (Δj) under different scan rates (d) (e) (f).

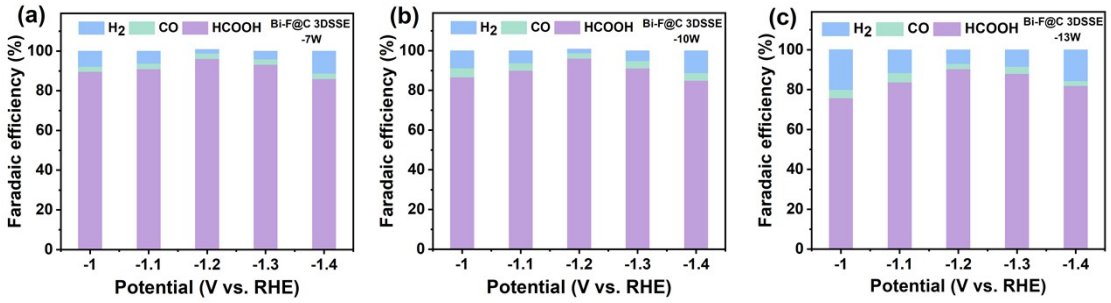

Figure S9. (a-c) Total faradaic efficiencies of products for Bi-F@C 3DSSE catalysts at applied potentials in the H-type cell.

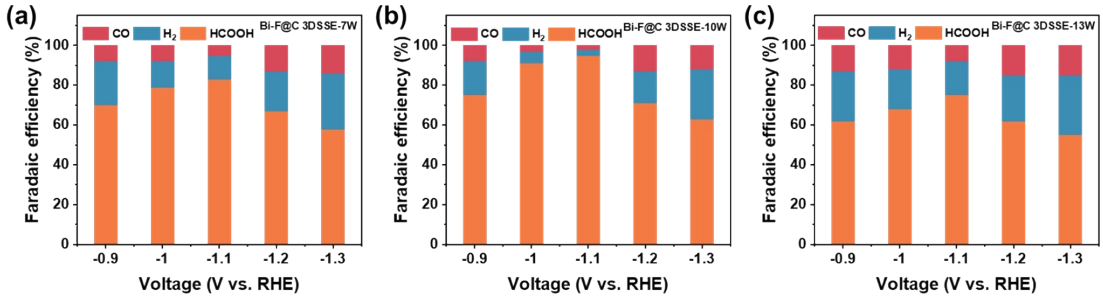

Figure S10. (a-c) Faradaic efficiencies of products over Bi-F@C 3DSSE in Flow cell (1M KOH).

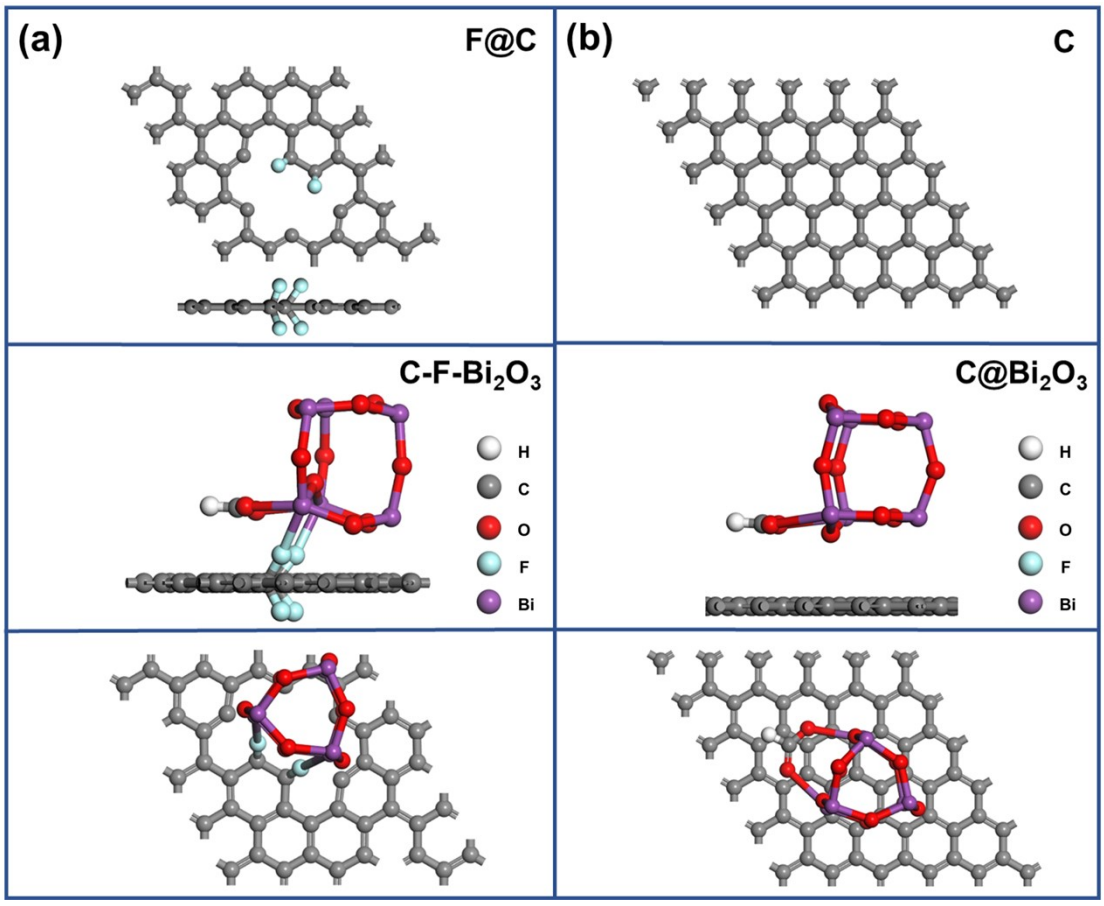

Figure S11. Optimized model of (a) HCOO*-Bi_2O_3-F-C and (b) HCOO*-Bi_2O_3@/C, in which red, blue, gray, and purple represent O, F, C, and Bi.

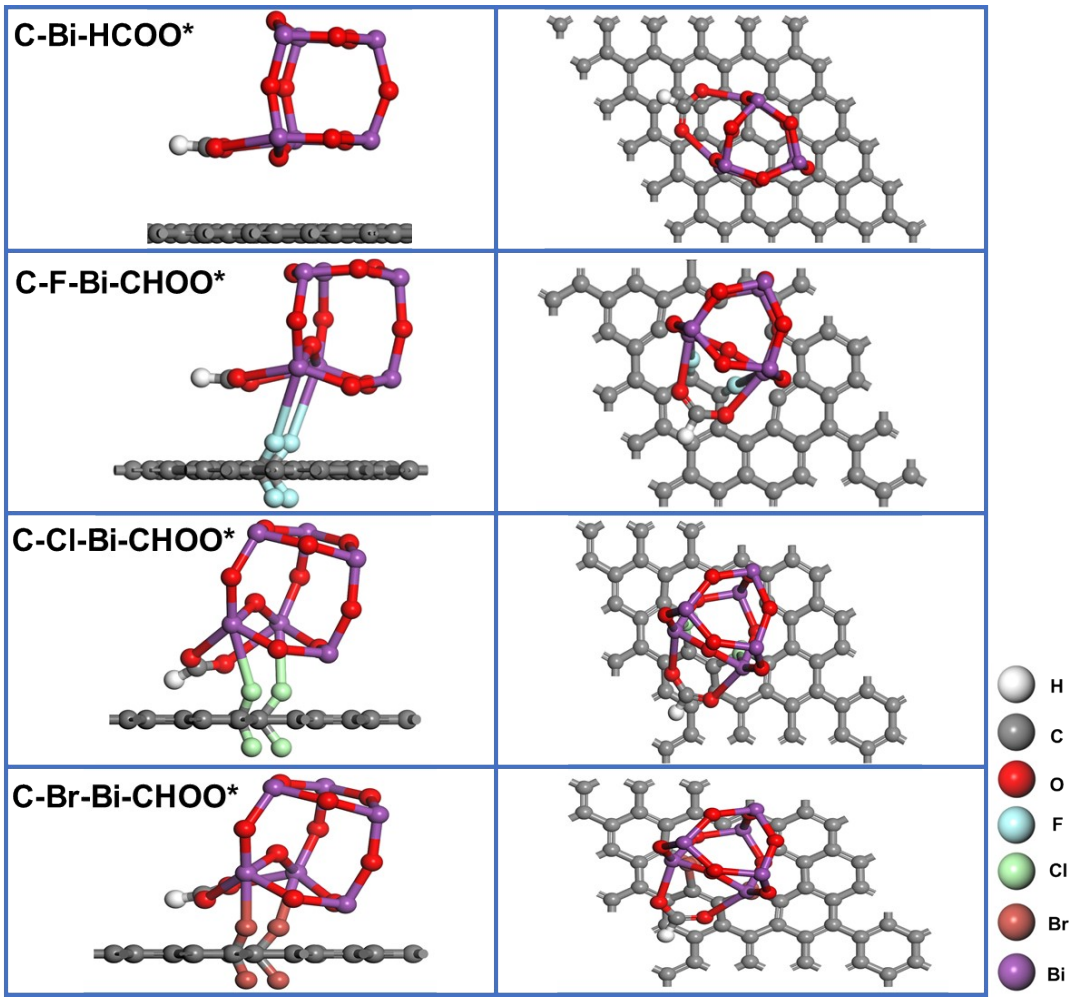

Figure S12. Optimized model of HCOO*-Bi_2O_3-F-C, HCOO*-Bi_2O_3-Cl-C, HCOO*-Bi_2O_3-Br-C and HCOO*-Bi_2O_3@/C.

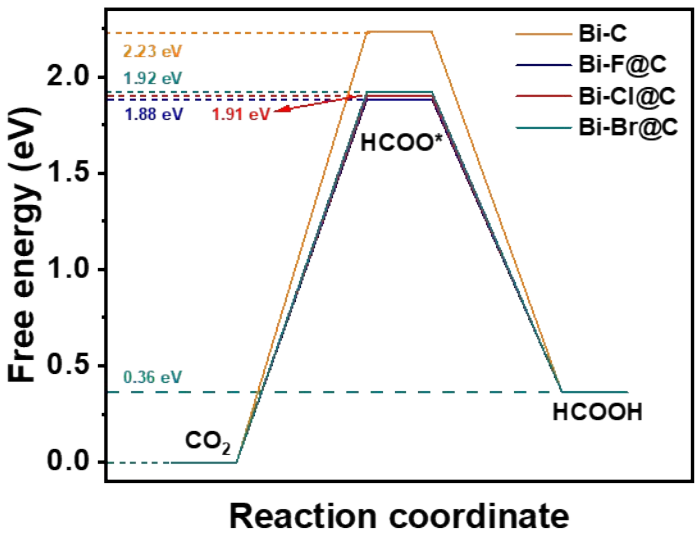

Figure S13. Free energy diagrams for CO_2RR to HCOOH on Bi_2O_3 connected with generating C-F-Bi bonds, C-Cl-Bi bonds, and C-Br-Bi bonds models.

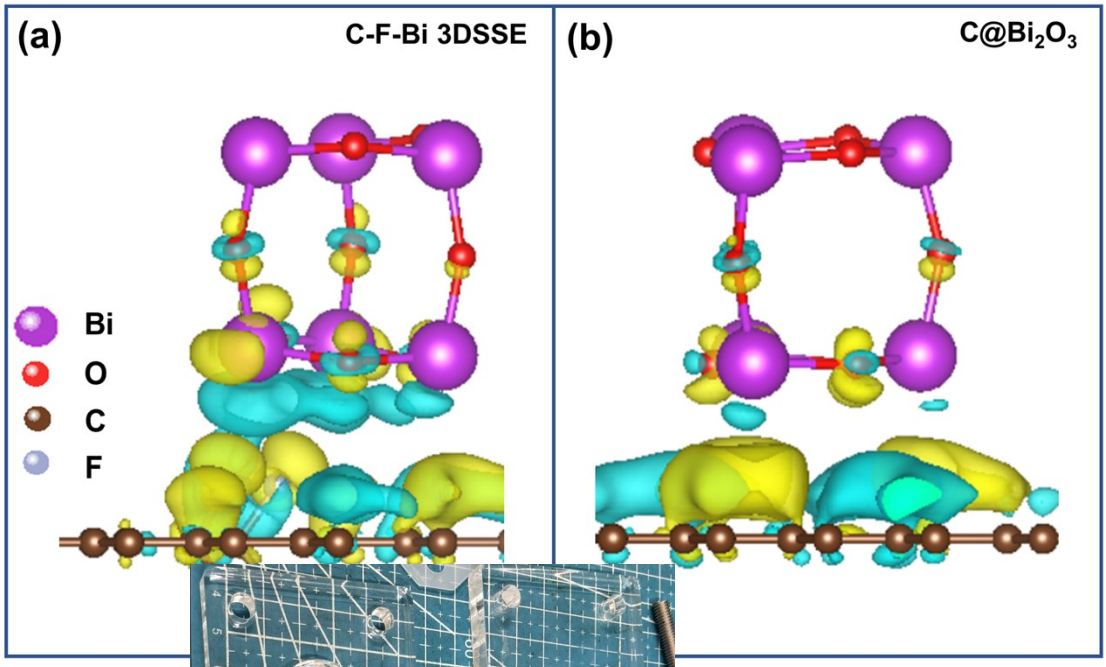

Figure S Bi_2O_3 and $C@Bi_2O_3$ catalysts.

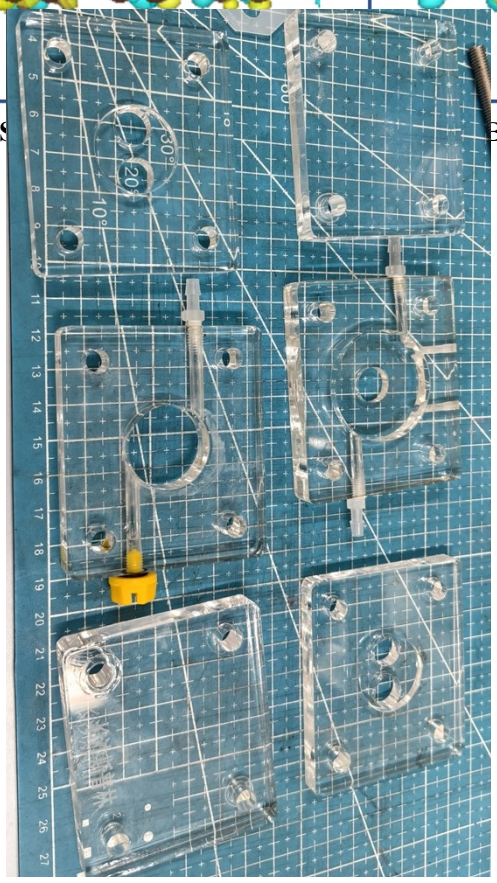

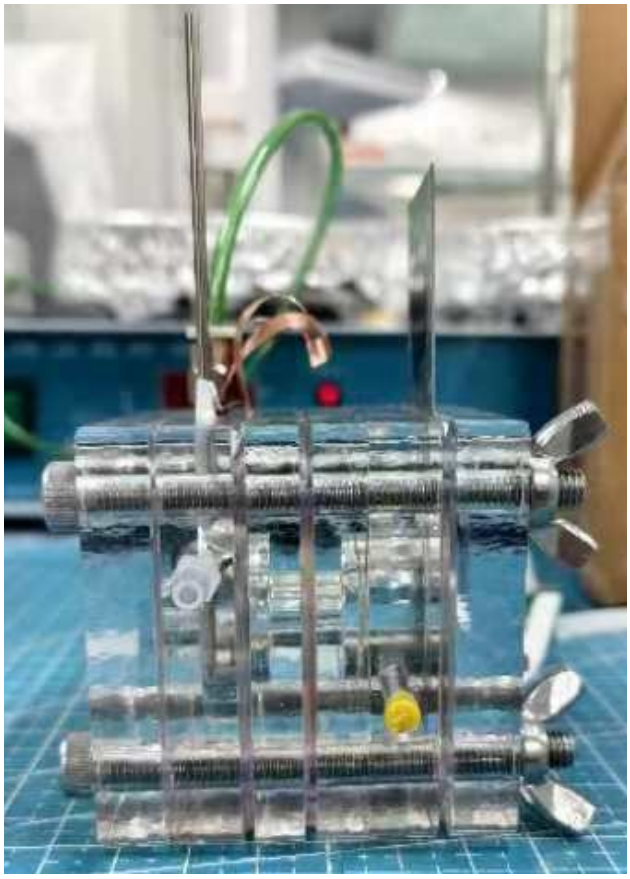

Figure S15. Schematic diagram of Zn-CO_2 battery components disassembled and Schematic diagram of Zn-CO_2 battery assembly.

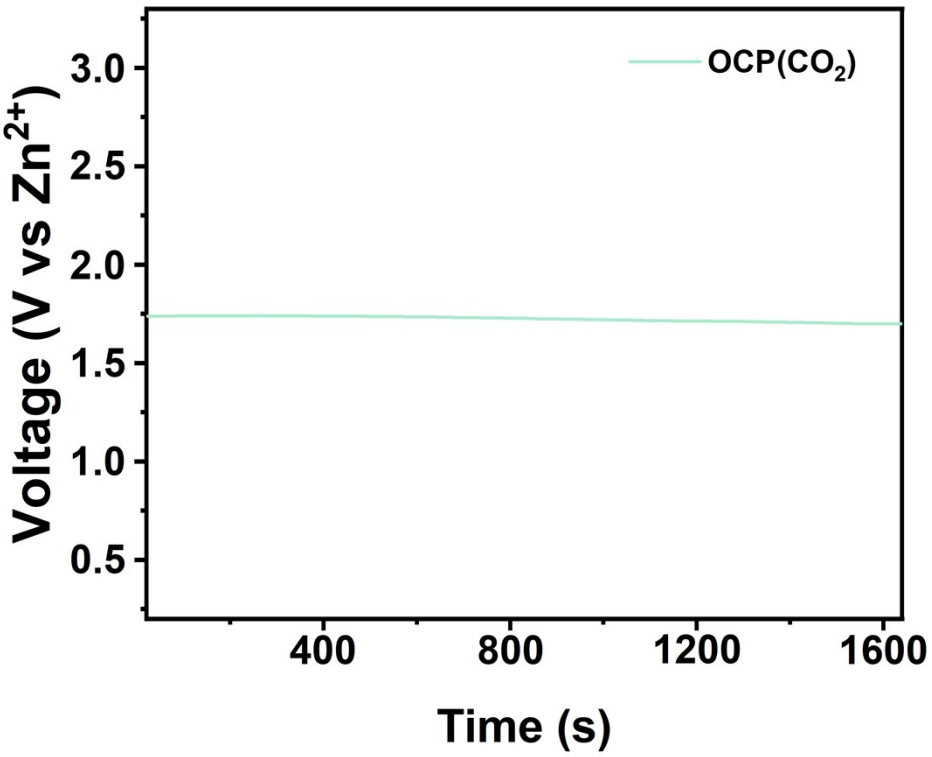

Figure S16. Open-circuit potential (OCP) exhibited by Zn–CO_2 batteries under continuous supply of carbon dioxide.

Table S1. Comparison of the activities of bismuth-based catalysts for CO_2 electroreduction to HCOOH.

Catalyst	Electrolyte	E (V vs RHE)	J (mA cm^{-2})	FE (%)	Reference
Bi-F@C 3DSSE	**0.1 M $KHCO_3$**	**-1.3**	**15**	**96**	**This Work**
	1 M KOH	**-1.1**	**231**	**97**	
D-Bi-NPS	0.1 M $KHCO_3$	-1.1	~11.5	94.1	ChemSusChem, 2025, 18, 00386.
Sn-3	0.1 M $KHCO_3$	-1.1	~68	87.8	Journal of Colloid and Interface Science, 2025, 700, 138576
Cu–Sn-1	0.1 M $KHCO_3$	-1.2	8	94.1	Journal of Environmental Chemical

					Engineering, 2025, 13, 118259
Bi-GDEs	2 M $KHCO_3$	-0.8	20	90	Catalysis Today, 2024, 437, 114743
Sn	0.1 M $KHCO_3$	-1.1	5	94	Chemical Engineering Journal, 2024, 482, 148972
Sb-SnS_2	0.1 M $KHCO_3$	-1.1	17.7	90.8	Journal of Industrial and Engineering Chemistry, 2023, 123, 33-40
In-NSs	1 M KOH	-1.1	50	96.3	ACS Nano, 2023, 17, 9338-9346
Co-$PbCO_3$ @CNs	0.1 M $KHCO_3$	-0.7	9.6	96.1	Applied Catalysis B: Environmental, 2023, 326, 122404
Bi_2O_3−CeOx	1 M KOH	-0.9	220	97	ACS Materials Letters 2022, 1749-1755
MIL-68	1 M KOH	-0.8	215	96	Nano-Micro Lett. 2022, 14, 167
Bi NTs	0.5 M $KHCO_3$	-1.1	39.4	93	ACS Catal., 2020, 10, 1, 358-364

4 References

1. D. E. McCoy, T. Feo, T. A. Harvey and R. O. Prum, *Nature Communications*, 2018, **9**, 1.
2. Z. Li, B. Sun, D. Xiao, Z. Wang, Y. Liu, Z. Zheng, P. Wang, Y. Dai, H. Cheng and B. Huang, *Angewandte Chemie International Edition*, 2023, **62**, e202217569.
3. Y. Pan, R. Lin, Y. Chen, S. Liu, W. Zhu, X. Cao, W. Chen, K. Wu, W.-C. Cheong, Y. Wang, L. Zheng, J. Luo, Y. Lin, Y. Liu, C. Liu, J. Li, Q. Lu, X. Chen, D. Wang, Q. Peng, C. Chen and Y. Li, *Journal of the American Chemical Society*, 2018, **140**, 4218-4221.
4. M. Thommes, K. Kaneko, A. V. Neimark, J. P. Olivier, F. Rodriguez-Reinoso, J. Rouquerol and K. S. W. Sing, *Pure and Applied Chemistry*, 2015, **87**, 1051-1069.
5. S. Trasatti and O. A. Petrii, *Pure and Applied Chemistry*, 1991, **63**, 711-734.
6. J. H. de Boer, B. C. Lippens, B. G. Linsen, J. C. P. Broekhoff, A. van den Heuvel and T. J. Osinga, *J. Colloid Interf. Sci.*, 1966, **21**, 405-414.

7. E. P. Barrett, L. G. Joyner and P. P. Halenda, *J. Am. Chem. Soc.*, 1951, **73**, 373-380.
8. X. Yuan, S. Chen, D. Cheng, L. Li, W. Zhu, D. Zhong, Z. J. Zhao, J. Li, T. Wang and J. Gong, *Angew. Chem. Int. Ed.*, 2021, **60**, 15344-15347.
9. B. Wei, Y. Xiong, Z. Zhang, J. Hao, L. Li and W. Shi, *Appl. Catal. B Environ.*, 2021, **283**, 119646.